

Article

Pyramid-Patterned Germanium Composite Film Anode for Rechargeable Lithium-Ion Batteries Prepared Using a One-Step Physical Method

Liyong Wang ^{1,†} , Mei Wang ¹, Liansheng Jiao ^{2,†}, Huiqi Wang ^{1,*}, Jinhua Yang ^{1,3}, Xiaozhong Dong ⁴, Ting Bi ¹, Shengsheng Ji ¹, Lei Liu ¹, Shengliang Hu ¹, Chengmeng Chen ⁵, Quanguo Guo ^{5,*} and Zhanjun Liu ^{5,*}

¹ School of Energy and Power Engineering, North University of China, Taiyuan 030001, China

² School of Chemistry and Chemical Engineering, Hebei Normal University for Nationalities, Chengde 067000, China

³ National Key Laboratory of Advanced Composites, AECC Beijing Institute of Aeronautical Materials, Beijing 100095, China

⁴ Department of Materials Engineering, Taiyuan Institute of Technology, Taiyuan 030001, China

⁵ CAS Key Laboratory of Carbon Materials, Institute of Coal Chemistry, Chinese Academy of Sciences, Taiyuan 030001, China

* Correspondence: hqiwang@nuc.edu.cn (H.W.); qgguo@sxicc.ac.cn (Q.G.); zjliu03@sxicc.ac.cn (Z.L.)

† These authors contributed equally to this work.

Abstract: Using a top-down magnetron sputtering technique with a high deposition-rate, a one-step method for preparing germanium (Ge) hybrid film is presented. At present, graphite film is used as a current collector because it is flexible, self lubricating, and possesses a stress–strain-relieving property. In order to further suppress the volume changes of the Ge, a multilayered electrically conductive nickel film is deposited between multilayered Ge films. The cells are cycled at a current density of 200 mA g⁻¹. An initial discharge and charge capacity of 1180.7 and 949.3 mAh g⁻¹ are achieved by the prepared integrated pyramid patterned Ge composite film anode, respectively. The average capacity was maintained at 580 mAh g⁻¹ after 280 cycles. In the rate capability measurement, the Ge composite demonstrated a reversible capacity of 1163.1 mAh g⁻¹. It is easily made using magnetron sputtering, which is widely accepted in the industry. A physical approach to increase pure Ge's specific capacity and its cycle life for LIBs is demonstrated in this work.

Keywords: germanium; graphite film; lithium-ion battery; magnetron sputtering



Citation: Wang, L.; Wang, M.; Jiao, L.; Wang, H.; Yang, J.; Dong, X.; Bi, T.; Ji, S.; Liu, L.; Hu, S.; et al.

Pyramid-Patterned Germanium Composite Film Anode for Rechargeable Lithium-Ion Batteries Prepared Using a One-Step Physical Method. *Coatings* **2023**, *13*, 555.

<https://doi.org/10.3390/coatings13030555>

Academic Editor: Je Moon Yun

Received: 18 November 2022

Revised: 26 February 2023

Accepted: 27 February 2023

Published: 5 March 2023



Copyright: © 2023 by the authors. Licensee MDPI, Basel, Switzerland. This article is an open access article distributed under the terms and conditions of the Creative Commons Attribution (CC BY) license (<https://creativecommons.org/licenses/by/4.0/>).

1. Introduction

One element with a relatively high abundance on the Earth's surface is germanium (Ge). It has special energy band structure, which is classified as a semiconductor. Based on this semiconductor characteristic, this element has been utilized in semiconductors, catalysts, optical fibers, and sensors [1–5]. Graphite has been commercially available for many years. Based on the application and study of carbon anodes, the ion storage mechanism was further revealed. It also aroused researchers' interest in studying other materials, such as silicon (Si), stannum, plumbum, etc. Ge has been also extended to the field of lithium-ion batteries (LIBs) as a result of the rapid advancement of science and technology [6–13].

Through the research of materials, these batteries finally turned into devices suitable for use in daily life. LIBs, which provide power for electric vehicles and personal computers and support a new energy generation, have sparked widespread public concern [14–19]. The LIBs' anode materials, which primarily consist of carbon materials, a semiconductor alloy, and metal oxide, play an important role. Though many factors affect the performance of the LIBs, numerous methods have been employed to improve their performance [20–29]. An artificial structure design of an anode material could optimize the original structure

of the materials, improving their specific capacity and cycle life. Theoretical simulation revealed the mechanism of anode materials in the discharge–charge process, which could provide a suggestion for material research and development. The theoretical capacity of graphite material is lower than that of the Ge ($\sim 1624 \text{ mAh g}^{-1}$), reaching 372 mAh g^{-1} . When Ge is used as anode material for LIBs, a serious issue arises. The volume of the Ge alloy formed with lithium-ions will increase to 300% of its natural volume, allowing for high specific capacity. Following a de-alloying process, the volume of the Ge-based alloy will shrink. Meanwhile, the Ge particles will clump together during the subsequent process, resulting in higher resistance and a longer diffusion path for lithium-ions [30–32]. To achieve high capacity and a relatively long cycle, it is important to address the negative aspects of Ge. A variety of methods and strategies have been employed to achieve the abovementioned objective. Ge can be prepared for use in nanoparticles, nanotubes, nanowires, and film, which display excellent cycling performances. Among the various methods, one that was used to improve electron transport and maintain the electrical contact in anode materials was the use of conductive additives [33,34]. In order to reduce volume changes, Ge nanoparticles could be combined with one-dimensional carbon nanostructures [35–38]. The one-dimensional carbon material provides good electrical conductivity along its length and could be grown on the current collectors. By electrospinning and then applying heat reduction, Ge clusters were enclosed in the nitrogen-doped carbon nanofibers. After 50 cycles, the prepared hybrids offered a capacity of $1266.7 \text{ mAh g}^{-1}$ at a current of 100 mA g^{-1} . The capacity marginally fell below average with an increase in the current. The capacity of the Ge hybrids was 938.6 mAh g^{-1} at 1 A g^{-1} for 50 cycles. The capacity was maintained at around 600 mAh g^{-1} , even when cycled at a current density of 8 A/g . The carbon nanofibers were used during the design process to provide superior electrical conductivity, as well as space for Ge clusters. The Ge clusters' hybrid anode's superior electrochemical characteristics were a result of this structure's design [39].

Due to its unique Dirac electronic band structure, high room temperature carrier mobility of $230,000 \text{ cm}^2/\text{V s}$, visible transparency of 97%, exceptional conductivity of 10^6 S/m , and thermal conductivity of 5000 W/m K , graphene has been used in a variety of industries in areas such as hydrogen storage, electronic devices such as transistors, and field emission displays [40–46]. With its high specific surface area, graphene has also been applied as an electrode material for electrochemical energy devices, such as batteries, supercapacitors, fuel cells and solar cells. The template-assisted in-situ reduction method was used to create the three-dimensional interconnected porous graphene [47]. Then, in order to be employed as anode materials, the Ge nanoparticles were equally distributed throughout the porous graphene. After 100 cycles, the synthesized Ge/porous graphene anode achieved a high capacity of 1102 mAh g^{-1} at 0.2 C . At a high electrical current of 5 C , it also had an excellent rate capacity of 494 mAh g^{-1} . The composites' three-dimensional porous graphene improved the materials' electronic conductivity and reaction kinetics, while also providing enough buffer area to minimize volume changes during the cycling and preserve the anode's structural integrity. Graphene with a different structure could improve the performance of the electrode materials. The flexible graphene framework, which served as an anode for LIBs, was distributed with Ge nanoparticles. In the first cycle, the nanocomposite exhibited a high Coulombic efficiency of 80.4%. With a capacity retention of 84.9% after 400 complete cycles, it demonstrated a reversible capacity of 675 mAh g^{-1} at a current density of 400 mA g^{-1} [48].

Non-carbon materials are also being studied in LIBs. Titanium dioxide (TiO_2) is a common material for solar cells and catalysts [49,50] and it is also used for Ge-based LIBs [51]. Dealloying of the GeTiAl ternary alloy in mild conditions made it easy to create a macroporous Ge skeleton that was wrapped by TiO_2 particles [52]. TiO_2 particles prevented the Ge skeleton from coming into direct contact with electrolytes by acting as an outer buffer wall for the Ge skeleton. The prepared anode's high reversible capacity of 774.8 mAh g^{-1} at 3.2 A/g after 300 cycles was optimal. Ge with a covering configuration could successfully mitigate its volume changes to drag out its cycle life and further develop

its electrochemical properties [53]. Using scalable ball milling, Ge-particles were embedded in the thin graphite nanoplatelets. After 200 cycles, the prepared anode had a capacity of 822 mAh g⁻¹ at 0.1 A/g.

The binder and conductive agent that were typically present in traditional Ge-based electrode materials had the potential to boost the stability and the electrical conductivity, but they also decreased the energy density of the whole [54–60]. The mass of the binder would occupy a certain proportion of that of the whole electrode, which could not provide energy storage. As a result, binder-free Ge-based anode material promised to elevate the electrochemical performance [19,31,61,62]. The nanostructure was created by electrochemical etching with hydrofluoric acid and plasma enhanced chemical vapor deposition of a Ge film onto the metallic substrate. After 1000 cycles, the binder-free Ge anode had a coulombic efficiency of 99.6% and a reversible capacity of 1300 mAh g⁻¹ at 1 C. The stability of the electrode could be attributed to the fact that Ge's film structure effectively dampened the volume fluctuations.

The analysis above suggests that the design of the nanostructure effectively enhanced the Ge's electrochemical properties. Additionally, the energy density of the whole electrode increased as a result of the anode material's decrease in the binding properties. In order to prepare Ge-based composites with a novel structure and enhance their electrochemical performance, it is desirable to combine the aforementioned methods. A top-down, high-deposition-rate method for producing a Ge hybrid film is presented in this paper in the form of a one-step procedure. The flexible and self-lubricating properties, as well as the good thermal and electrical conductivity of graphite film could also help alleviate stress-strain properties. Magnetron sputtering, which is capable of successfully preparing metal and semiconductor films, was used to deposit Ge on the graphite film substrate. The Ge's volume fluctuation could be effectively mitigated by using a film pattern. A layered structure was created to further suppress the Ge's volume fluctuations. First, a graphite film substrate was coated with a nickel film, and then the nickel film was coated with a Ge film. A nickel film sandwiched between the Ge film and the graphite substrate could not only effectively connect the two, but also lessen the impact of volume changes.

The morphology of the prepared Ge composite film's cross-section resembled pyramids. Cycled at a current density of 200 mA g⁻¹, initial discharge and charge capacities of 1180.7 and 949.3 mAh g⁻¹ were achieved by the pyramid-shaped Ge composite film anode, respectively. After 280 cycles, it maintained an average capacity of over 580 mAh g⁻¹. The preparation did not contain many complicated chemical reactions because of the physical method. In this study, a physical approach to enhance pure Ge's specific capacity and lifecycle for LIBs was demonstrated.

2. Experimental Section

2.1. Raw Materials and Methods

The graphite film was treated at 3073 K under argon atmosphere in the graphitization furnace. Its average thickness was about 25 μm. The Ge target material was purchased from Beijing Goodwill Metal Technology Co., Ltd. (Beijing, China) with a purity of 99.999%. The nickel target material had a purity of 99.995%.

The designed composites were prepared via magnetron sputtering equipment, which was provided by the SKY technology development Co., Ltd. (Shenyang, China), Chinese Academy of Sciences.

The density functional theory (DFT) was applied to simulate the adsorption behavior of Li ion on the surface of anode materials, as implemented in the Vienna ab initio simulation package (VASP). The projector augmented wave (PAW) method was adopted to describe the interactions between ions and electrons. The generalized gradient approximation (GGA) in the form of Perdew, Burke, and Ernzerhof (PBE) was used to describe electron exchange and correlation. The plane-wave cutoff was set to 400 eV. The Brillouin zones were sampled with 2 × 2 × 1 Monkhorst-Pack meshes. The structures were fully relaxed until the maximum force on each atom was less than −0.05 eV Å⁻¹ and 10⁻⁵ eV. A vacuum

space of at least 15 Å was inserted along the z direction to avoid any interactions between the periodically repeated images. The van der Waals interaction has been considered using the DFT-D₃ scheme.

2.2. Characterizations and Electrochemical Evaluation

Field-emission scanning electron microscopy (SEM, JSM-7001F) and field-emission transmission electron microscopy (TEM, JEM-2100F) were used to observe the microstructure of the samples. The microstructure of the samples was also studied by the Raman spectra (HORIBA Jobin Yvon, LabRam HR800, $\lambda = 532$ nm). X-ray photoelectron spectroscopy (XPS) was performed with a Kratos Axis Ultra DLD spectrometer equipped with a monochromatic Al K α source (15 Kv, 20 mA).

CR 2016-type coin cells were assembled in a glovebox with Ar atmosphere. Li foil was used as the counter electrode and reference electrode, with microporous polypropylene film (Celgard 2400, South Lakes Drive, Charlotte, NC, USA) as the separator. The electrolyte was composed of 1 M LiPF₆ in ethylene carbonate-dimethyl carbonate (1:1 by volume) and 5 vol.% vinylene carbonate. The cells were galvanostatically discharged and charged using a battery test system (LAND CT 2001A model, Wuhan Jinnuo Electronics Ltd., Wuhan, China) in the voltage range of 0.01–2 V at room temperature. The electrochemical workstation was purchased from Shanghai Chenhua Instrument Co., Ltd. (Shanghai, China) (CHI660E).

3. Results and Discussion

The Vienna Ab Initio Simulation Package (VASP) was used to apply the DFT calculations to theoretically analyze the lithium-ion storage of the Ge and carbon material. In Figure 1a,b, the 0 eV position represents the Fermi energy level. Figure 1b depicts the density of states (DOS) curves of Ge, carbon, and lithium. At the Fermi energy level position, the DOS of the Ge–lithium alloy was higher than that of the carbon–lithium alloy. Figure 1c,d demonstrates the optimized geometry structure of pure Ge and carbon structures with lithium-ion. The Li⁺ adsorption energies of the pure Ge and carbon structures were −0.1379 eV and 0.7821 eV, respectively, indicating the Ge had higher affinity toward Li⁺.

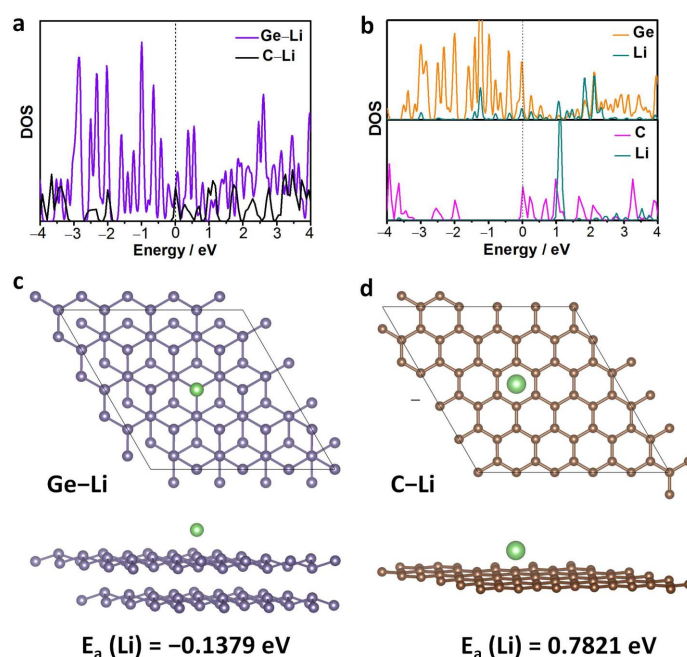


Figure 1. DFT analysis: (a) DOS of the Ge–lithium and carbon–lithium alloy; (b) DOS of the Ge, carbon, and lithium; (c,d) optimized geometry structure of pure Ge and carbon structures. The green atoms represent lithium atoms. The brown atoms represent carbon atoms. The dark blue atoms represent Ge atoms.

In view of the DFT calculation, an advanced novel construction of nano Ge/graphite composite film was prepared using magnetron sputtering equipment. Figure 2 depicts a one-step procedure for preparing a pyramid-patterned germanium composite film anode. The nickel material was first deposited on the graphite film with 10 watts for 5 min. Then, the Ge material was deposited on the nickel film with 18 watts for 10 min. According to the sequence above, a series of experiments were performed. Finally, the nickel material was deposited on the upper Ge film with 10 watts for 5 min, which covered the whole film. During the experimental process, the working gas was argon gas with a purity of 99.999% at room temperature. The prepared Ge composite film was used as the anode material for the LIBs.

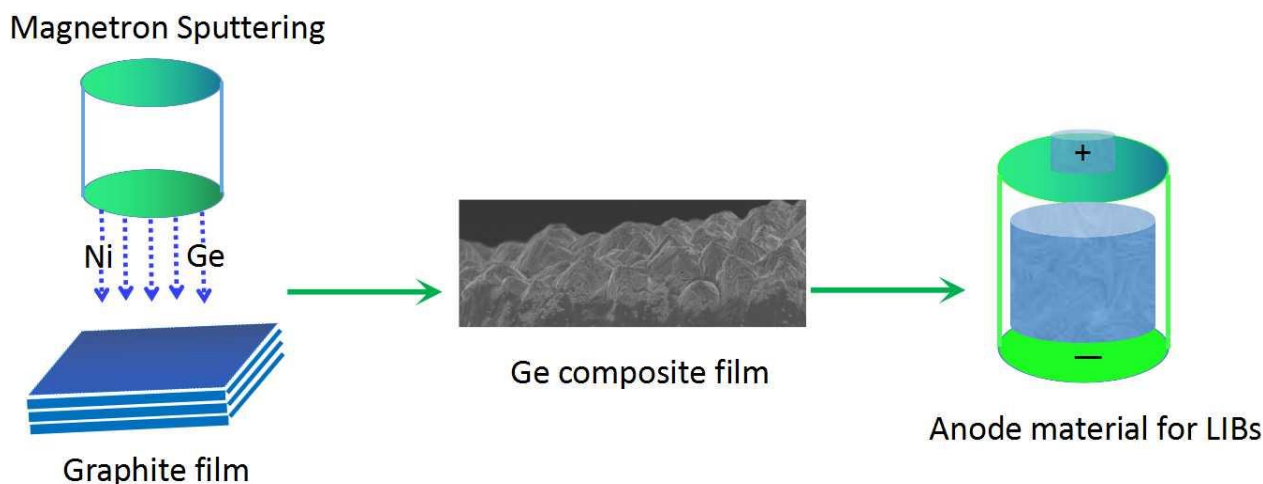


Figure 2. Schematic illustration of the fabrication process of the pyramid-patterned Ge film anode by magnetron sputtering.

Thus far, the anode material generally used for LIBs is graphite, which is resistant to acid, alkali, and corrosion [20,63]. Graphite powder can provide a capacity of 370 mAh/g for LIBs. The anode composites' current collector can be made of graphite film because of its good electrical conductivity [64,65]. Figure 3a displays the obvious layer structure of the cross-sectional part of the graphite film. The layers of graphite were tightly stacked. Figure 3b mainly contains a carbon element, after the line scanning test along the yellow line of Figure 3a. In Figure 3c, the surface appearance of the graphite film looks like clouds.

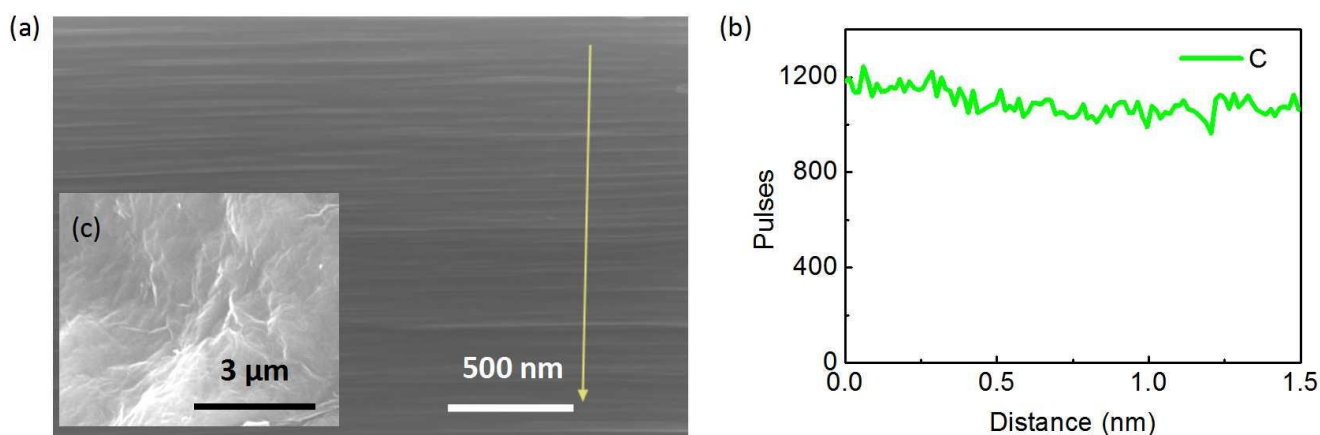


Figure 3. SEM images: (a) the cross-section of the graphite film, (b) the line scanning test, and (c) the surface of the graphite film.

In order to prepare the Ge composite film anode, the Ge and nickel were designed and grown on the graphite film. The nickel had strong interfacial bonding with Ge and graphite [66–71]. The nickel was first deposited on the graphite film. Then, the Ge was deposited on the nickel film. As per the arrangement above, 25 tests were carried out. Once again, the nickel was deposited on the upper Ge film, which covered the whole film. The surface appearance of the prepared sample is shown in Figure 4a,b. It seemed as though there were many particles on the surface. With the increase in the magnification, the particles are clearly observed in Figure 4c,d. They have the appearance of pyramids, which is an undulating and closely connected arrangement. There is a clear connection between the smaller pyramid and the larger pyramid nearby. The pyramids had a nickel coating on their surface, which was the result of the most recent nickel deposit.

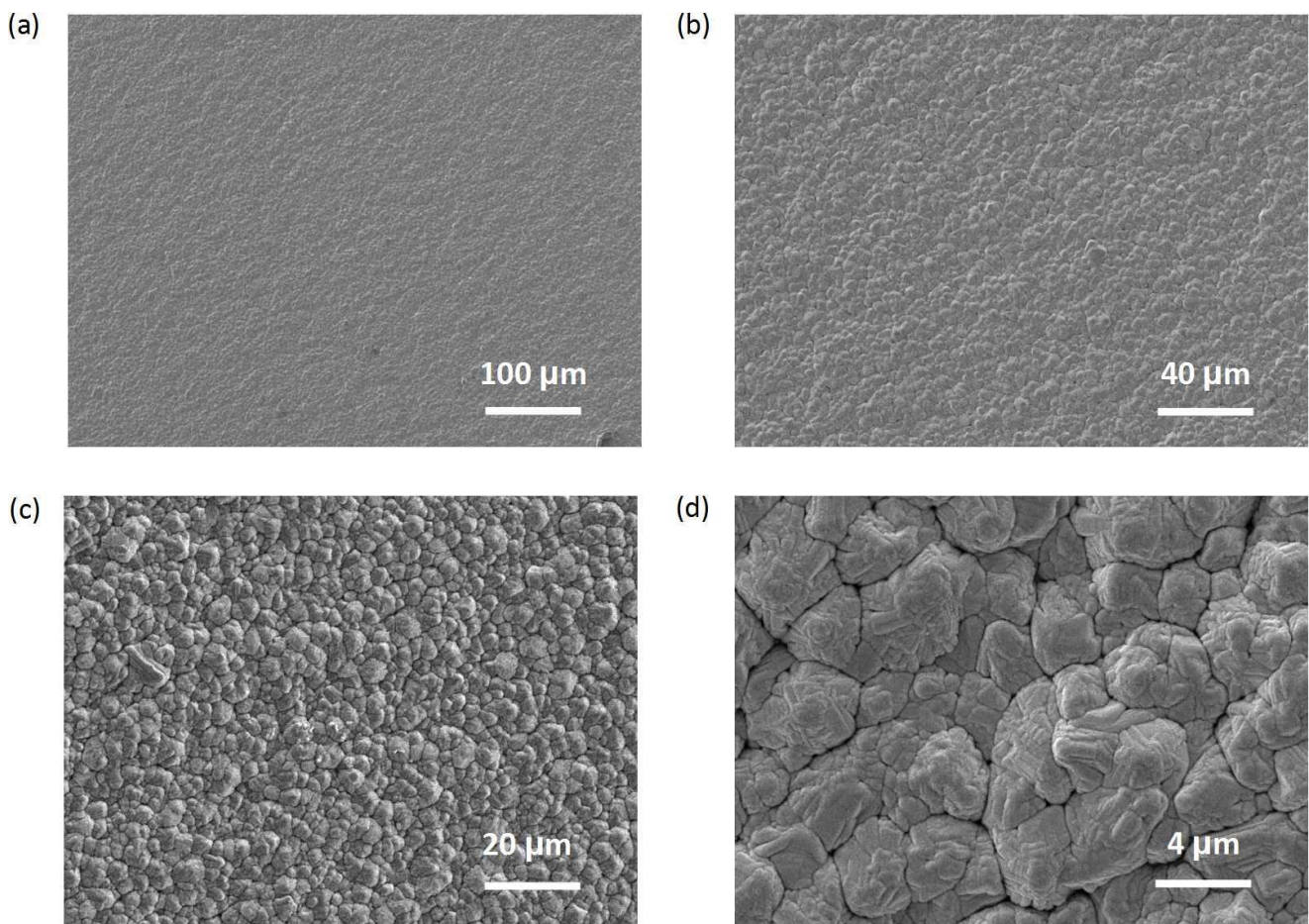


Figure 4. SEM images of surface Ge composite film with different magnification: (a) 200 times, (b) 500 times, (c) 1000 times, and (d) 5000 times.

The map scanning was used in the SEM test to find all the elements in Figure 5a. The components are depicted in Figure 5b. Many different-colored dots joined together. The Ge element is represented by the red dots in Figure 5c. The green dots represent the carbon element in Figure 5d, which matched the graphite film. The nickel element is represented by the blue dots in Figure 5e. In Figure 5f, each element's presence indicates distinct peak patterns. The three components were equally distributed across the whole area. The experiment's design was supported by the aforementioned outcomes.

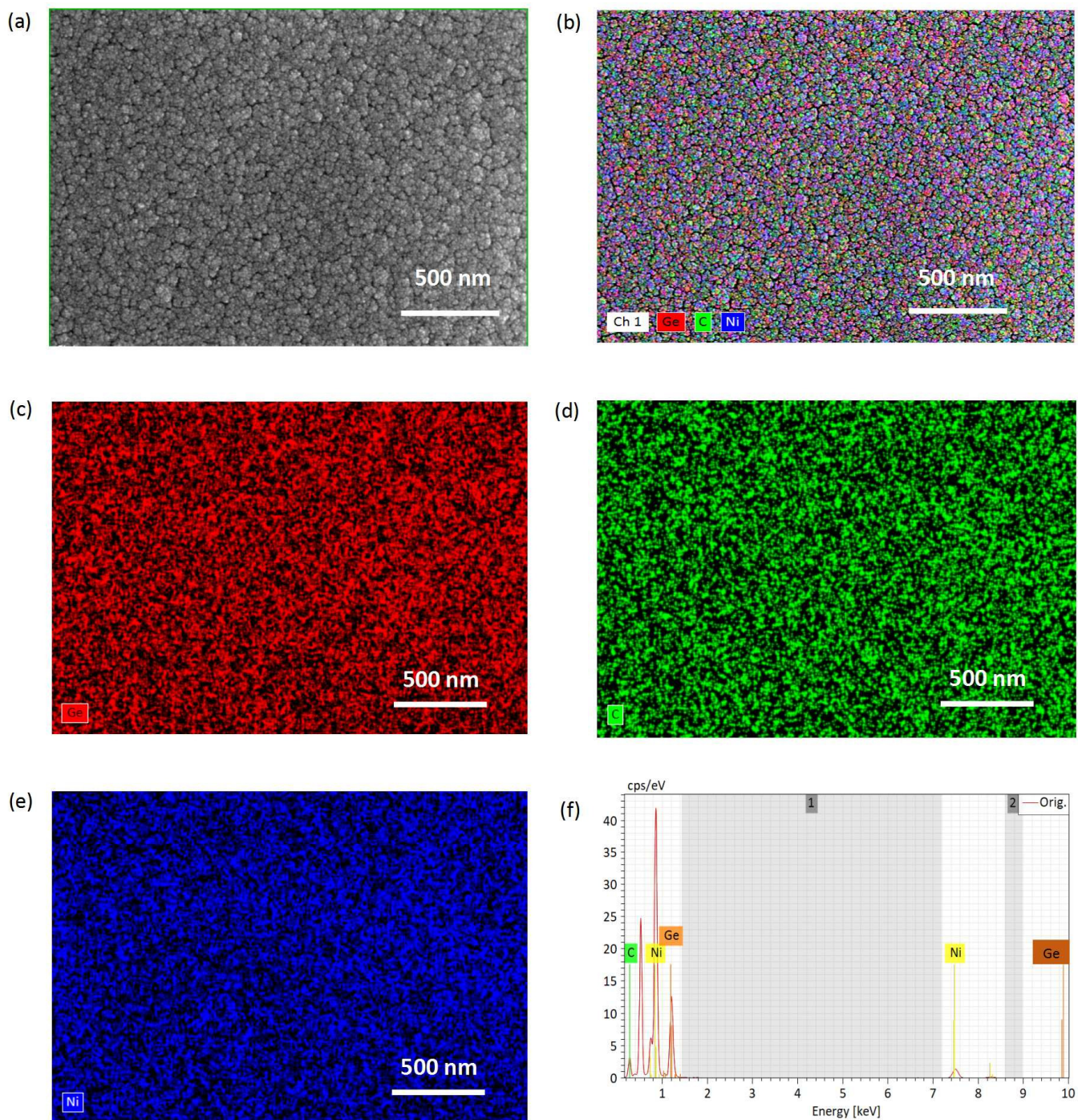


Figure 5. SEM images: (a) the surface part of the Ge composite film, (b) the mapping pattern of Figure 3a, (c) the Ge element distribution map, (d) the carbon element distribution map, (e) the nickel element distribution map, and (f) the element mapping of the Ge, carbon, and nickel.

The various magnification images were chosen to examine the transverse section of the Ge composite film. In Figure 6a, the transverse of the Ge composite film is slim, and the piece of film was curled up. In Figure 6b, the upper light-colored part of the material is the Ge composite film, and the dark-colored part is the graphite film substrate. The appearance of the Ge composite film is similar to pyramids with well-spaced distribution in Figure 6c. As depicted in Figure 6d, the pyramids adhered well to the graphite film without showing any phase separation. It also indicates that the graphite film had been

combined with the Ge composite film. This was beneficial to the structural stability of the integrative composite material used as anode material for LIBs.

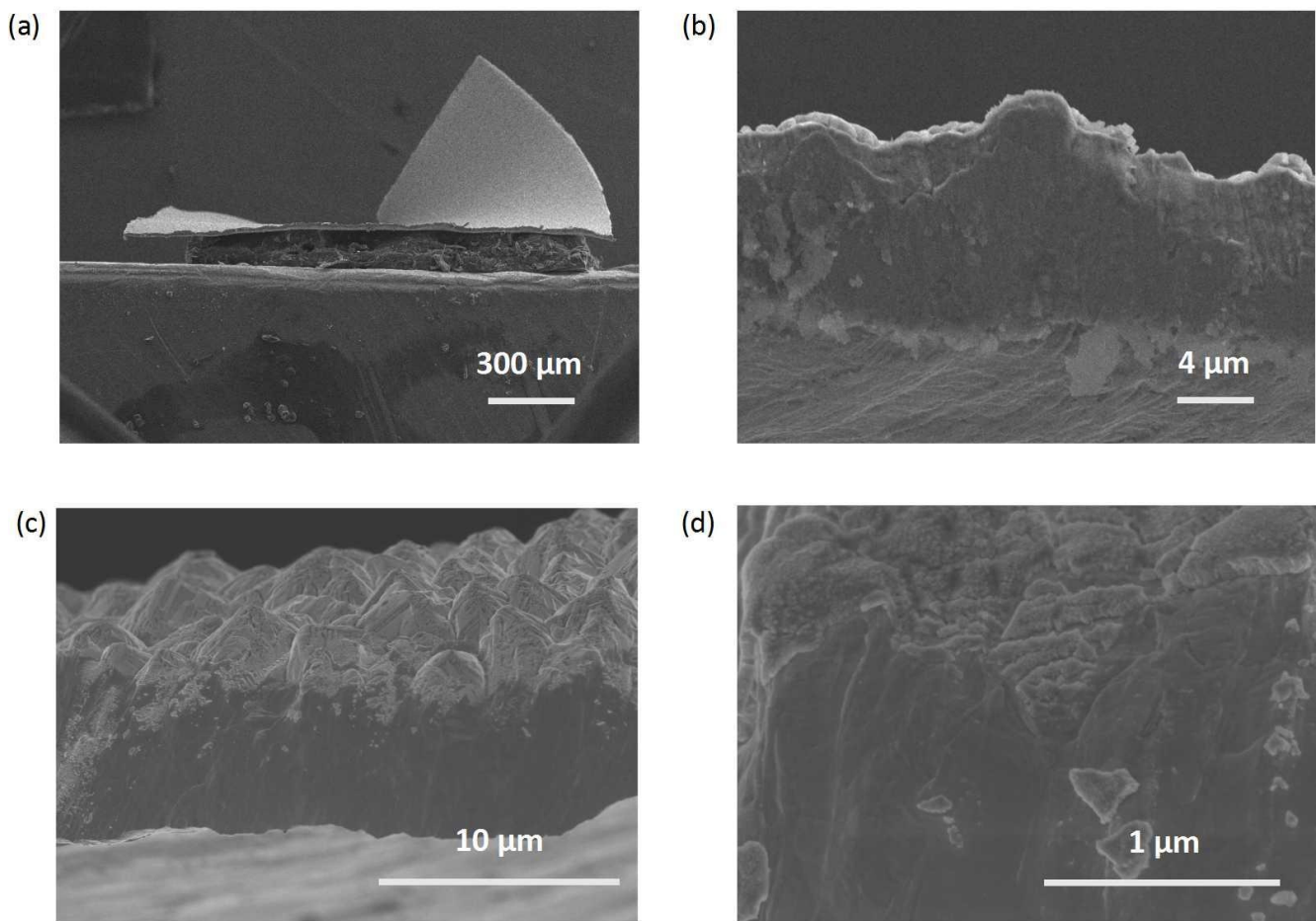


Figure 6. SEM images: (a,b) the transverse section of the Ge composite film with low magnification and (c,d) the pyramids pattern of Figure 4a with high magnification.

The Ge composite film was grown on the graphite film using nickel as a binder. The results of TEM test are exhibited in Figure 7a. Its mapping analysis covered the entire area. The nickel is represented by the green dots. The Ge is represented by the red part of the sample in Figure 7c. The blue dots represent the graphite film substrate in Figure 7d. Once again, this confirmed that the prepared samples contained graphite, nickel, and Ge. Additionally, it was possible to draw the conclusion that the structure design of the Ge composite film that was growing on the graphite was feasible. The integrated hybrid resulted in good structural stability, which helped reduce the material's stress–strain impact.

The prepared sample's crystallite was identified using Raman spectroscopy, as shown in Figure 8a. In the composite in Figure 8b, the Ge peaked at 262.98 cm^{-1} [30,38,72]. The nickel played a role in the apex at 536.4 cm^{-1} . Pyramid-patterned Ge/nickel film was deposited on the graphite film. The Raman was sensitive to the upper Ge/nickel film of the Ge composite material. The signal of the Ge and Ni was strong in the Raman spectra. The height of the pyramids was not uniform. The bigger pyramids were on the scale of about a few hundred nanometers. Thus, the carbon signal was relatively weaker than that of the Ge/nickel film. In Figure 8c, the carbon peak can be observed at 1574.01 cm^{-1} , which was related to the graphite film [73].

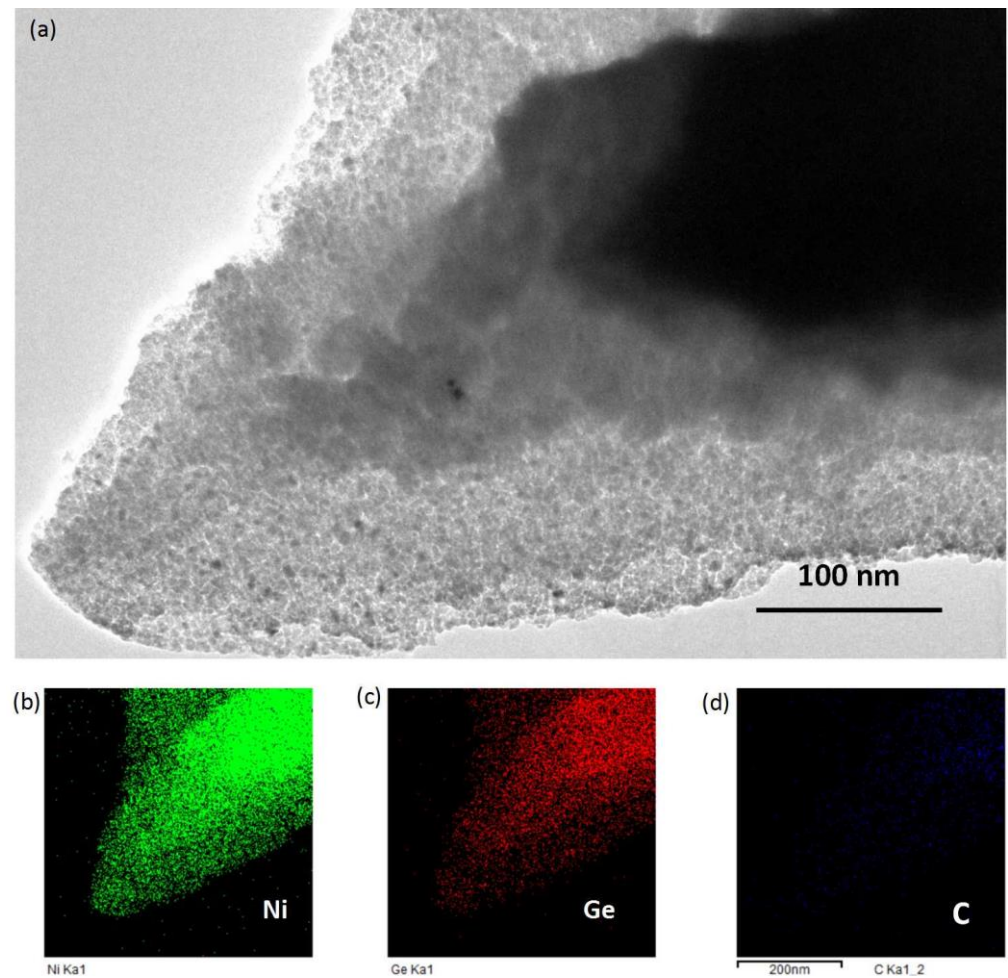


Figure 7. TEM images: (a) the Ge composite film growing on the graphite, (b) the nickel element distribution map, (c) the Ge element distribution map, and (d) the carbon element distribution map.

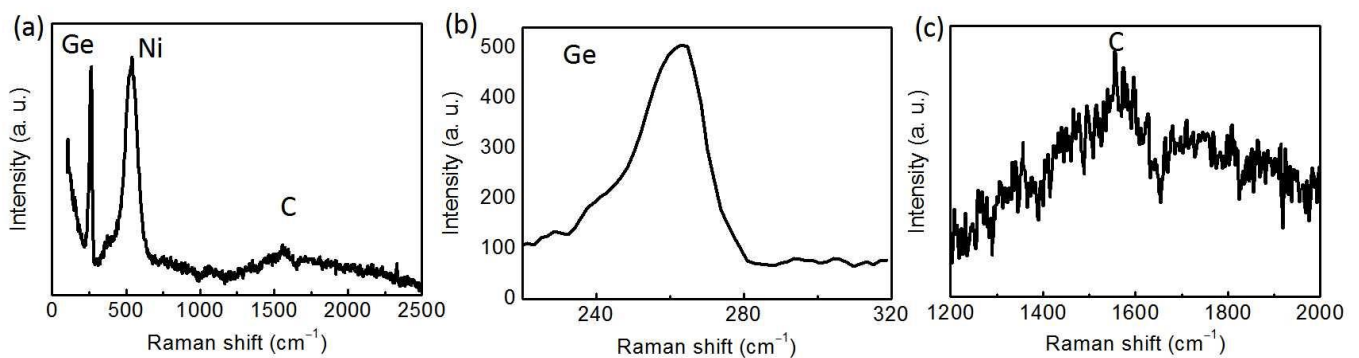


Figure 8. Raman spectra of the Ge composite film (a), Raman spectra of the Ge (b), and Raman spectra of the graphite (c).

The XPS survey of the Ge composite film developing on the graphite is shown in Figure 9a. It is the Ge 3d peak at 32.38 eV in the Figure 9b [52]. At 184.08 eV, the Ge 3s peak underwent testing. At 125.08 eV, the Ge 3p peak was identified. Additionally, the Ge 2p peak matched the peak of 1251.08 eV [39]. The manufactured samples' graphite substrate, as shown in Figure 9c, was related to the C 1s peak at 284.78 eV [74,75]. As depicted in Figure 9d, the Ni 2p peak was observed at an energy of 855.68 eV [68,76]. The aforementioned findings showed that the three types of elements' XPS characteristic peaks

agreed with the basic composite material design scheme. There was no other material involved in the final composite.

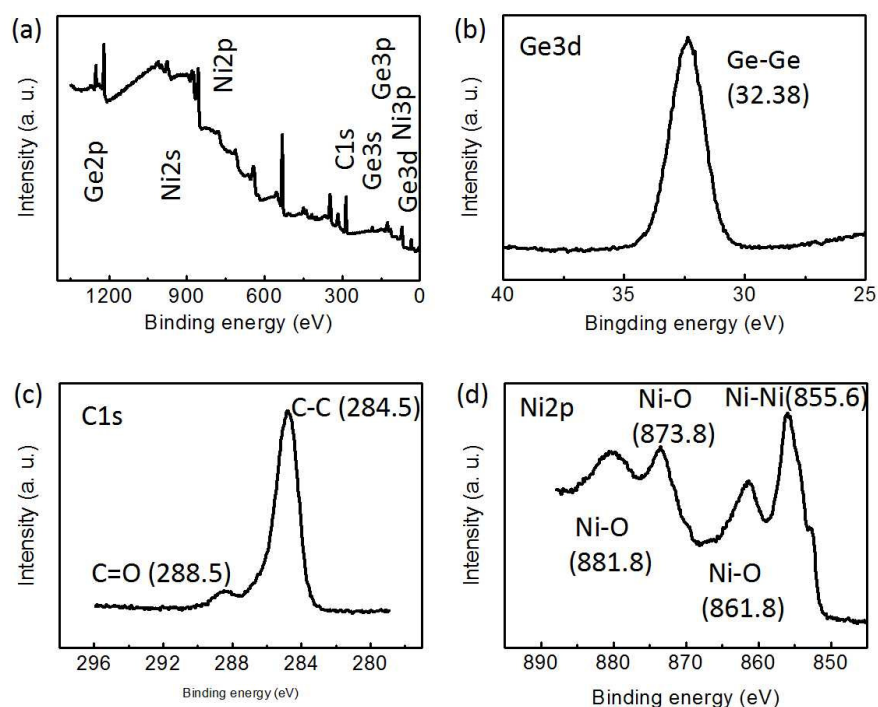


Figure 9. XPS survey: (a) the Ge composite film growing on the graphite, (b) the Ge 3d peak, (c) the C 1s peak, and (d) the Ni 2p peak.

As shown in Figure 10a, the cycle performance of the Ge composite film was tested at a current density of 200 mA g^{-1} . The diameter of the graphite film collector was 16 mm. The average mass loading was 0.37 milligrams, which included the Ge film and nickel film. The initial discharge and charge capacities of the Ge composite film electrode were 1180.7 and 949.3 mAh g^{-1} , respectively, with a Coulombic efficiency of 80.4% (Figure 10c). The first discharge energy density was 494.5 Wh/kg and the first charge energy density was 686.1 Wh/kg . Without chemical bonding, the Ge composite had physical bonding. The Ge composite had full volume expansion/contraction when cycled at low current density, repeatedly producing the SEI. The SEI became comparatively stable after about 30 cycles, and the reversible capacity was reduced to around 600 mAh g^{-1} . Then, the Ge composite maintained an average capacity of over 580 mAh g^{-1} after 280 cycles.

In the Ge composite, the graphite film was used as a substrate for Ge film to grow on in addition to being employed as a negative current collector. The good flexible and self-lubricating properties of the graphite film substrate lessened the negative impacts of stress and strain caused by the volume change of the Ge materials, and successively prevented shedding between the active material and the collector. In order to increase the stability of the material, the nickel film was chosen as a metal binder between the graphite film and the Ge film. Both the graphite and nickel exhibited strong electrical conductivity, which improved the conductivity of the whole material. The multilayered nickel between the Ge films effectively alleviated the volume changes, improving the structural stability. In order to reduce the contact between the Ge and electrolyte, the Ge composite material was coated by the nickel layer during the final procedure. The integrated Ge composite film electrode's electrochemical performance was enhanced jointly by the aforementioned comprehensive measures. The only equipment used to prepare the composites was magnetron sputtering. Additionally, the Ge-based composite film was prepared with few chemical reactions.

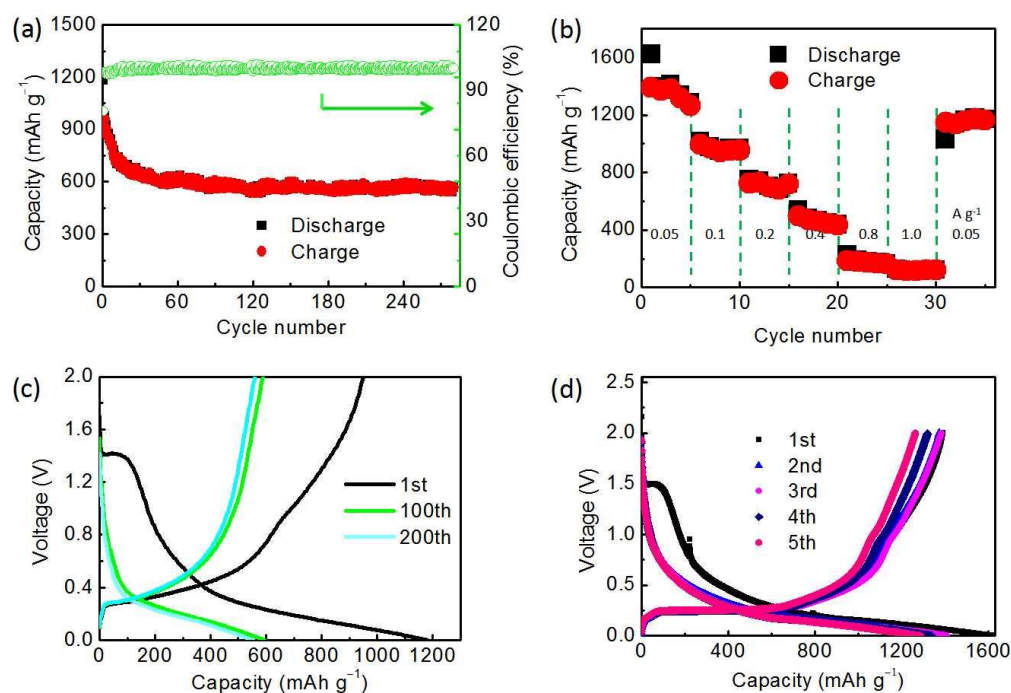


Figure 10. (a) Cycle performance of the Ge composite film. (b) Rate capability of the Ge composite film. The discharge—charge curves of the germanium composite film (c) at a current density of 0.2 A g⁻¹ and (d) at a current density of 0.05 A g⁻¹.

In order to effectively execute the discharge—charge cycles, the Ge was able to expand and contract in nature, thanks to its thin composite film structure. As the cycle number increased, a stable cycle stage was indicated by the obvious overlap in the capacity—voltage curves, as depicted in Figure 10c.

For the use of LIBs in power applications, rate capability is a crucial factor. It was found that the corresponding rate capability with the various stepwise rates increased from 50 mA g⁻¹ to 1000 mA g⁻¹ and then switched back. The Ge composite film delivered the reversible capacity of 1262.7, 954.5, and 720 mAh g⁻¹ after 5, 10, and 15 cycles, respectively. The reversible capacity started to decrease as the current densities increased. At the densities of 800 and 1000 mA g⁻¹, the Ge composite film obtained the reversible capacity of 164 and 122.8 mAh g⁻¹, respectively (Figure 10b). The Ge composite film electrode tested at 50 mA g⁻¹ had a reversible capacity of 1163.1 mAh g⁻¹ following the high-rate measurements, which was close to the value of the fifth cycle. The data above demonstrate that the Ge composite film is a suitable anode material for LIBs due to its high rate capability. As shown in Figure 10d, the first five capacity—voltage curves were tested at 50 mA g⁻¹. The first reversible capacity of the Ge composite was 1389.6 mAh g⁻¹. The voltage platform was about 0.24 V, corresponding to half of the reversible charging capacity.

Figure 11 depicts a typical cyclic voltammetry (CV) measurement of the Ge composite film electrode in the voltage range of 0.01–2.0 V at a sweep rate of 1 mV/s. During its cathodic half-cycle, the cathodic peak was clearly observed at a potential of 1.2 V, as shown in Figure 11a. This possibly resulted from the formation of the SEI film. In the anodic scan, there were obvious anodic peaks appearing at 0.51, 1.11, and 1.56 V. This might have resulted from the structure and component of the anode material. After the first activation cycle, the electrode material was relatively stable. After the next two cycles, the peak potential shifted to 0.49, 1.06, and 1.56 V, which overlapped quite well. During the second and third scan, the anodic peak potential (0.49 V) was very close to cathodic peak potential (0.53 V). A good electrochemical performance was demonstrated by the fact that the corresponding peaks and curves overlapped well during the subsequent scan.

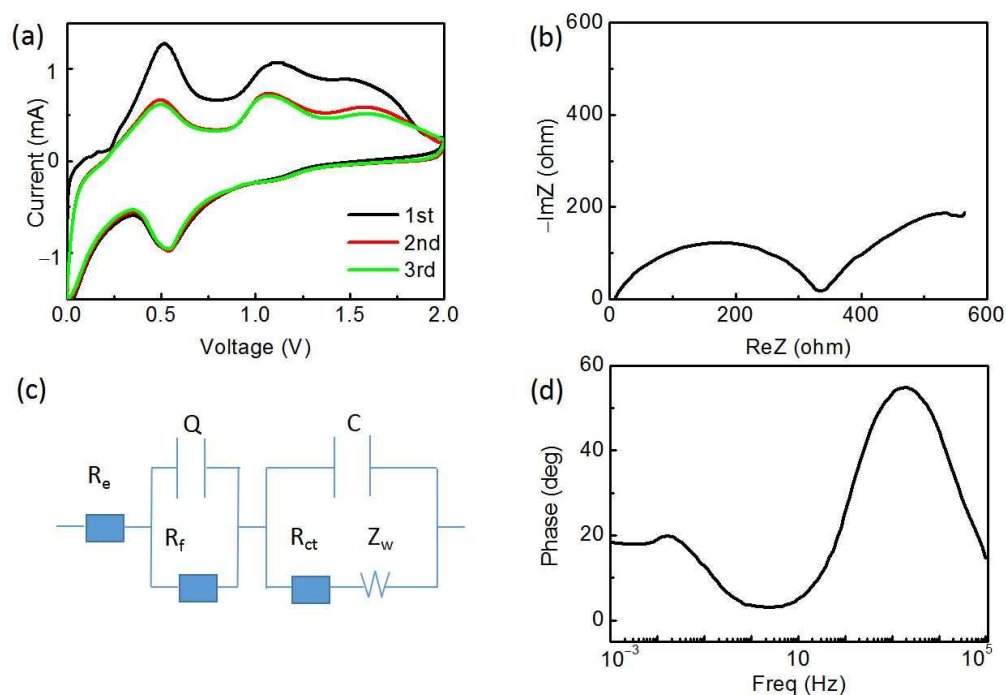


Figure 11. (a) Cyclic voltammetry curves, (b) Nyquist plots of the Ge composite, (c) equivalent circuit, and (d) the relationship between phase and frequency.

As shown in Figure 11b, the electrochemical impedance spectroscopy (EIS) measurements confirmed the electrical conductivity of the Ge composite film [77]. The electrochemical impedance measurements were performed at an AC voltage of 5 mV amplitude in the 100 KHz to 0.001 Hz range. A semicircle and a straight short sloping line made up the EIS spectra. The semicircle at the high-frequency region might result from the formation of the SEI. The straight short sloping line at low frequency was mainly related to the lithium diffusion impedance. The straight diffusion tail suggested that the Ge composite film facilitated the diffusion and transport of lithium-ions between the electrode and the electrolyte, reducing the lithium-ion diffusion resistance. The equivalent circuit is demonstrated in Figure 11c, where C represents the capacitance, R_e is the electrolyte resistance, R_{ct} represents the charge transfer resistance, Z_w represents the Warburg impedance, R_f represents the resistance of the surface film and contact, and Q represents the constant phase angle element. The values of R_{ct} and R_f were about 330 and 40 ohm, respectively. The nickel layer covered the whole surface of the anode material, which made it difficult for the electrolytes to wet the electrode material. Additionally, the Ge was a semiconductor, which had lower electronic conductivity compared with that of the good conductor. In the prepared Ge composite film, both the graphite film and nickel film had good electrical conductivity, enhancing the electrical conductivity of the entire electrode. As shown in Figure 11d, it had a protruding peak in the high frequency region, which was related to the first semicircle in the Nyquist plots. In the medium frequency region, this peak probably resulted from the interfacial charge transfer impedance. The lithium-ion diffusion usually corresponded to the low frequency.

4. Conclusions

In conclusion, a top-down method of high deposition-rate magnetron sputtering was used to prepare the Ge hybrid film in a single step. The pyramid-patterned Ge composite film anode delivered an initial discharge and charge capacity of 1180.7 and 949.3 mAh g⁻¹, respectively, which was tested at a current density of 200 mA g⁻¹. The reversible average capacity was over 580 mAh g⁻¹ after 280 cycles. It also had good rate capability. The Ge composite returned to its reversible capacity of 1163.1 mAh g⁻¹ at a current density of

50 mA g⁻¹. For LIBs, this work demonstrates a physical approach to improve the specific capacity and cycle life of pure Ge.

Author Contributions: L.W.: Design of the work, drafting the work, final approval of the version. M.W., T.B. and S.J.: Analysis. X.D. and L.J.: Design of the work. S.H., C.C. and L.L.: Acquisition. Z.L., Q.G. and J.Y.: Conception of the work. H.W.: Agreement to be accountable for all aspects of the work. All authors have read and agreed to the published version of the manuscript.

Funding: This work was supported by the Fundamental Research Program of Shanxi Province (No. 20210302123052, 201901D211270), the Key Research and Development (R&D) Projects of Shanxi Province (No. 202102040201003), and the Graduate Student Education Innovation Projects of Shanxi Province (No. 2020SY352, 2020SY355).

Institutional Review Board Statement: Not applicable.

Informed Consent Statement: Not applicable.

Data Availability Statement: Data is contained within the article.

Conflicts of Interest: The authors declare no conflict of interest.

References

1. Tao, J.; Tao, Z.; Zhihong, L. Review on resources and recycling of germanium, with special focus on characteristics, mechanism and challenges of solvent extraction. *J. Clean. Prod.* **2021**, *294*, 126217. [\[CrossRef\]](#)
2. Sanchez-Perez, C.; Garcia, I.; Rey-Stolle, I. Fast chemical thinning of germanium wafers for optoelectronic applications. *Appl. Surf. Sci.* **2022**, *579*, 152199–152202. [\[CrossRef\]](#)
3. Sicchieri, N.B.; Chiquito, A.J.; Gouveia, R.C. Electronic and optoelectronic properties of intrinsic and cooper-doped germanium nanowire network devices. *Mater. Today Proc.* **2022**, *51*, 1872–1877. [\[CrossRef\]](#)
4. Vanlalawmpuia, K.; Mitra, S.K.; Bhowmick, B. An analytical drain current model of Germanium source vertical tunnel field effect transistor. *Micro Nanostruct.* **2022**, *165*, 207197. [\[CrossRef\]](#)
5. Wang, P.; Chen, L.-Y.; Ge, J.-P.; Cai, W.; Chen, W.-Q. Incorporating critical material cycles into metal-energy nexus of China's 2050 renewable transition. *Appl. Energy* **2019**, *253*, 113612. [\[CrossRef\]](#)
6. Wei, Z.; Hu, J.; Li, Y.; He, H.; Li, W.; Sauer, D.U. Hierarchical soft measurement of load current and state of charge for future smart lithium-ion batteries. *Appl. Energy* **2022**, *307*, 118246. [\[CrossRef\]](#)
7. Cheng, F.; Liang, J.; Tao, Z.; Chen, J. Functional Materials for Rechargeable Batteries. *Adv. Mater.* **2011**, *23*, 1695–1715. [\[CrossRef\]](#)
8. Wandt, J.; Freiberg, A.T.S.; Ogrodnik, A.; Gasteiger, H.A. Singlet oxygen evolution from layered transition metal oxide cathode materials and its implications for lithium-ion batteries. *Mater. Today* **2018**, *21*, 825–833. [\[CrossRef\]](#)
9. Liang, S.; Cheng, Y.-J.; Zhu, J.; Xia, Y.; Müller-Buschbaum, P. A Chronicle Review of Nonsilicon (Sn, Sb, Ge)-Based Lithium/Sodium-Ion Battery Alloying Anodes. *Small Methods* **2020**, *4*, 2000218. [\[CrossRef\]](#)
10. Greenidge, G.; Erlebacher, J. Porous graphite fabricated by liquid metal dealloying of silicon carbide. *Carbon* **2020**, *165*, 45–54. [\[CrossRef\]](#)
11. Susantyoko, R.A.; Wang, X.; Sun, L.; Pey, K.L.; Fitzgerald, E.; Zhang, Q. Germanium coated vertically-aligned multiwall carbon nanotubes as lithium-ion battery anodes. *Carbon* **2014**, *77*, 551–559. [\[CrossRef\]](#)
12. Mishra, K.; George, K.; Zhou, X.-D. Submicron silicon anode stabilized by single-step carbon and germanium coatings for high capacity lithium-ion batteries. *Carbon* **2018**, *138*, 419–426. [\[CrossRef\]](#)
13. Gao, C.; Kim, N.D.; Villegas Salvatierra, R.; Lee, S.-K.; Li, L.; Li, Y.; Sha, J.; Silva, G.A.L.; Fei, H.; Xie, E.; et al. Germanium on seamless graphene carbon nanotube hybrids for lithium ion anodes. *Carbon* **2017**, *123*, 433–439. [\[CrossRef\]](#)
14. Ye, Y.; Chou, L.-Y.; Liu, Y.; Wang, H.; Lee, H.K.; Huang, W.; Wan, J.; Liu, K.; Zhou, G.; Yang, Y.; et al. Ultralight and fire-extinguishing current collectors for high-energy and high-safety lithium-ion batteries. *Nat. Energy* **2020**, *5*, 786–793. [\[CrossRef\]](#)
15. Duffner, F.; Kronemeyer, N.; Tübke, J.; Leker, J.; Winter, M.; Schmich, R. Post-lithium-ion battery cell production and its compatibility with lithium-ion cell production infrastructure. *Nat. Energy* **2021**, *6*, 123–134. [\[CrossRef\]](#)
16. Román-Ramírez, L.A.; Marco, J. Design of experiments applied to lithium-ion batteries: A literature review. *Appl. Energy* **2022**, *320*, 119305. [\[CrossRef\]](#)
17. Lander, L.; Kallitsis, E.; Hales, A.; Edge, J.S.; Korre, A.; Offer, G. Cost and carbon footprint reduction of electric vehicle lithium-ion batteries through efficient thermal management. *Appl. Energy* **2021**, *289*, 116737. [\[CrossRef\]](#)
18. Yang, L.; Cai, Y.; Yang, Y.; Deng, Z. Supervisory long-term prediction of state of available power for lithium-ion batteries in electric vehicles. *Appl. Energy* **2020**, *257*, 114006. [\[CrossRef\]](#)
19. Li, P.; Kim, H.; Kim, K.-H.; Kim, J.; Jung, H.-G.; Sun, Y.-K. State-of-the-art anodes of potassium-ion batteries: Synthesis, chemistry, and applications. *Chem. Sci.* **2021**, *12*, 7623–7655. [\[CrossRef\]](#)
20. Meng, C.; Yuan, M.; Cao, B.; Lin, X.; Zhang, J.; Li, A.; Chen, X.; Jia, M.; Song, H. Laser-modified graphitic onion-like carbon as anode for lithium/potassium-ion batteries. *Carbon* **2022**, *192*, 347–355. [\[CrossRef\]](#)

21. Wang, H.-Q.; Zhao, Y.-X.; Gou, L.; Wang, L.-Y.; Wang, M.; Li, Y.; Hu, S.-L. Rational construction of densely packed Si/MXene composite microspheres enables favorable sodium storage. *Rare Met.* **2022**, *41*, 1626–1636. [[CrossRef](#)]
22. Wang, H.; An, D.; Tian, P.; Jing, W.; Wang, M.; Li, Y.; Li, H.-R.; Hu, S.; Ye, T.-N. Incorporating quantum-sized boron dots into 3D cross-linked rGO skeleton to enable the activity of boron anode for favorable lithium storage. *Chem. Eng. J.* **2021**, *425*, 130659. [[CrossRef](#)]
23. Ma, C.-L.; Hu, Z.-H.; Song, N.-J.; Zhao, Y.; Liu, Y.-Z.; Wang, H.-Q. Constructing mild expanded graphite microspheres by pressurized oxidation combined microwave treatment for enhanced lithium storage. *Rare Met.* **2021**, *40*, 837–847. [[CrossRef](#)]
24. Wang, L.; Liu, Z.; Guo, Q.; Wang, G.; Yang, J.; Li, P.; Wang, X.; Liu, L. Electrochemical properties of carbon nanocoils and hollow graphite fibers as anodes for rechargeable lithium ion batteries. *Electrochim. Acta* **2016**, *199*, 204–209. [[CrossRef](#)]
25. Liu, N.; Huo, K.; McDowell, M.T.; Zhao, J.; Cui, Y. Rice husks as a sustainable source of nanostructured silicon for high performance Li-ion battery anodes. *Sci. Rep.* **2013**, *3*, 1919. [[CrossRef](#)]
26. Zhou, L.; Zhang, J.; Wu, Y.; Wang, W.; Ming, H.; Sun, Q.; Wang, L.; Ming, J.; Alshareef, H.N. Understanding Ostwald Ripening and Surface Charging Effects in Solvothermally-Prepared Metal Oxide–Carbon Anodes for High Performance Rechargeable Batteries. *Adv. Energy Mater.* **2019**, *9*, 1902194. [[CrossRef](#)]
27. Fang, R.; Chen, K.; Yin, L.; Sun, Z.; Li, F.; Cheng, H.-M. The Regulating Role of Carbon Nanotubes and Graphene in Lithium-Ion and Lithium–Sulfur Batteries. *Adv. Mater.* **2019**, *31*, 1800863. [[CrossRef](#)]
28. Alain, M.; Haiming, X.; Christian, M.J. Composite anodes for lithium-ion batteries: Status and trends. *AIMS Mater. Sci.* **2016**, *3*, 1054–1106. [[CrossRef](#)]
29. Chang, H.-H.; Ho, T.-H.; Su, Y.-S. Graphene-Enhanced Battery Components in Rechargeable Lithium-Ion and Lithium Metal Batteries. *C* **2021**, *7*, 65. [[CrossRef](#)]
30. Li, D.; Wang, H.; Zhou, T.; Zhang, W.; Liu, H.K.; Guo, Z. Unique Structural Design and Strategies for Germanium-Based Anode Materials Toward Enhanced Lithium Storage. *Adv. Energy Mater.* **2017**, *7*, 1700488. [[CrossRef](#)]
31. Fugattini, S.; Gulzar, U.; Andreoli, A.; Carbone, L.; Boschetti, M.; Bernardoni, P.; Gjestila, M.; Mangherini, G.; Camattari, R.; Li, T.; et al. Binder-free nanostructured germanium anode for high resilience lithium-ion battery. *Electrochim. Acta* **2022**, *411*, 139832. [[CrossRef](#)]
32. David, L.; Ruther, R.E.; Mohanty, D.; Meyer, H.M.; Sheng, Y.; Kalnaus, S.; Daniel, C.; Wood, D.L. Identifying degradation mechanisms in lithium-ion batteries with coating defects at the cathode. *Appl. Energy* **2018**, *231*, 446–455. [[CrossRef](#)]
33. Joey, D.O. Invited review: High Energy Density Germanium Anodes for Next Generation Lithium Ion Batteries. *Appl. Chem. Eng.* **2014**, *25*, 1–13.
34. Bogart, T.D.; Chockla, A.M.; Korgel, B.A. High capacity lithium ion battery anodes of silicon and germanium. *Curr. Opin. Chem. Eng.* **2013**, *2*, 286–293. [[CrossRef](#)]
35. Liu, J.; Song, K.; Zhu, C.; Chen, C.-C.; van Aken, P.A.; Maier, J.; Yu, Y. Ge/C Nanowires as High-Capacity and Long-Life Anode Materials for Li-Ion Batteries. *ACS Nano* **2014**, *8*, 7051–7059. [[CrossRef](#)] [[PubMed](#)]
36. Gavrilin, I.M.; Kudryashova, Y.O.; Kuz'mina, A.A.; Kulova, T.L.; Skundin, A.M.; Emets, V.V.; Volkov, R.L.; Dronov, A.A.; Borgardt, N.I.; Gavrilov, S.A. High-rate and low-temperature performance of germanium nanowires anode for lithium-ion batteries. *J. Electroanal. Chem.* **2021**, *888*, 115209. [[CrossRef](#)]
37. Wang, T.; Xie, G.; Zhu, J.; Lu, B. Elastic Reduced Graphene Oxide Nanosheets Embedded in Germanium Nanofiber Matrix as Anode Material for High-Performance Li-Ion Battery. *Electrochim. Acta* **2015**, *186*, 64–70. [[CrossRef](#)]
38. DiLeo, R.A.; Ganter, M.J.; Thone, M.N.; Forney, M.W.; Staub, J.W.; Rogers, R.E.; Landi, B.J. Balanced approach to safety of high capacity silicon–germanium–carbon nanotube free-standing lithium ion battery anodes. *Nano Energy* **2013**, *2*, 268–275. [[CrossRef](#)]
39. Wang, W.; Xiao, Y.; Wang, X.; Liu, B.; Cao, M. In Situ Encapsulation of Germanium Clusters in Carbon Nanofibers: High-Performance Anodes for Lithium-Ion Batteries. *ChemSusChem* **2014**, *7*, 2914–2922. [[CrossRef](#)]
40. Chen, C.; Yang, Q.-H.; Yang, Y.; Lv, W.; Wen, Y.; Hou, P.-X.; Wang, M.; Cheng, H.-M. Self-Assembled Free-Standing Graphite Oxide Membrane. *Adv. Mater.* **2009**, *21*, 3007–3011. [[CrossRef](#)]
41. Bertolazzi, S.; Bondavalli, P.; Roche, S.; San, T.; Choi, S.-Y.; Colombo, L.; Bonaccorso, F.; Samori, P. Nonvolatile Memories Based on Graphene and Related 2D Materials. *Adv. Mater.* **2019**, *31*, 1806663. [[CrossRef](#)] [[PubMed](#)]
42. You, R.; Liu, Y.-Q.; Hao, Y.-L.; Han, D.-D.; Zhang, Y.-L.; You, Z. Laser Fabrication of Graphene-Based Flexible Electronics. *Adv. Mater.* **2020**, *32*, 1901981. [[CrossRef](#)] [[PubMed](#)]
43. Huang, H.; Yan, M.; Yang, C.; He, H.; Jiang, Q.; Yang, L.; Lu, Z.; Sun, Z.; Xu, X.; Bando, Y.; et al. Graphene Nanoarchitectonics: Recent Advances in Graphene-Based Electrocatalysts for Hydrogen Evolution Reaction. *Adv. Mater.* **2019**, *31*, 1903415. [[CrossRef](#)] [[PubMed](#)]
44. Chen, B.; Zhong, X.; Zhou, G.; Zhao, N.; Cheng, H.-M. Graphene-Supported Atomically Dispersed Metals as Bifunctional Catalysts for Next-Generation Batteries Based on Conversion Reactions. *Adv. Mater.* **2022**, *34*, 2105812. [[CrossRef](#)]
45. Chen, Z.; Qi, Y.; Chen, X.; Zhang, Y.; Liu, Z. Direct CVD Growth of Graphene on Traditional Glass: Methods and Mechanisms. *Adv. Mater.* **2019**, *31*, 1803639. [[CrossRef](#)]
46. Wang, K.; Hui, K.N.; San Hui, K.; Peng, S.; Xu, Y. Recent progress in metal–organic framework/graphene-derived materials for energy storage and conversion: Design, preparation, and application. *Chem. Sci.* **2021**, *12*, 5737–5766. [[CrossRef](#)] [[PubMed](#)]

47. Chen, Y.; Zou, Y.; Shen, X.; Qiu, J.; Lian, J.; Pu, J.; Li, S.; Du, F.-H.; Li, S.-Q.; Ji, Z.; et al. Ge nanoparticles uniformly immobilized on 3D interconnected porous graphene frameworks as anodes for high-performance lithium-ion batteries. *J. Energy Chem.* **2022**, *69*, 161–173. [[CrossRef](#)]
48. Ren, J.-G.; Wu, Q.-H.; Tang, H.; Hong, G.; Zhang, W.; Lee, S.-T. Germanium–graphene composite anode for high-energy lithium batteries with long cycle life. *J. Mater. Chem. A* **2013**, *1*, 1821–1826. [[CrossRef](#)]
49. Haider, A.; Ali, G.; Haider, M.J.; Edan, M.S.; Al-Obaidy, R.; Thamir, A.; Hathal, M.M.; Abbas, E.M.; Al-Sheikh, F. Modification optical properties of TiO₂ nanostructure as solar cell. *Energy Rep.* **2022**, *8*, 77–85. [[CrossRef](#)]
50. Tashkandi, N.Y.; Albukhari, S.M.; Ismail, A.A. Mesoporous TiO₂ enhanced by anchoring Mn₃O₄ for highly efficient photocatalyst toward photo-oxidation of ciprofloxacin. *Opt. Mater.* **2022**, *127*, 112274. [[CrossRef](#)]
51. Ren, H.; Sun, J.; Yu, R.; Yang, M.; Gu, L.; Liu, P.; Zhao, H.; Kisailus, D.; Wang, D. Controllable synthesis of mesostructures from TiO₂ hollow to porous nanospheres with superior rate performance for lithium ion batteries. *Chem. Sci.* **2016**, *7*, 793–798. [[CrossRef](#)] [[PubMed](#)]
52. Liu, Q.; Hou, J.; Xu, C.; Chen, Z.; Qin, R.; Liu, H. TiO₂ particles wrapped onto macroporous germanium skeleton as high performance anode for lithium-ion batteries. *Chem. Eng. J.* **2020**, *381*, 122649. [[CrossRef](#)]
53. Sultana, I.; Rahman, M.M.; Glushenkov, A.M.; Mateti, S.; Tanwar, K.; Huang, S.; Chen, Y. Nano germanium incorporated thin graphite nanoplatelets: A novel germanium based lithium-ion battery anode with enhanced electrochemical performance. *Electrochim. Acta* **2021**, *391*, 139001. [[CrossRef](#)]
54. Wang, Q.; Wu, X.; You, H.; Min, H.; Xu, X.; Hao, J.; Liu, X.; Yang, H. Template-directed Prussian blue nanocubes supported on Ni foam as the binder-free anode of lithium-ion batteries. *Appl. Surf. Sci.* **2022**, *571*, 151194. [[CrossRef](#)]
55. Zhai, J.; Lei, Z.; Sun, K.; Zhu, S. MXene enabled binder-free FeOF cathode with high volumetric and gravimetric capacities for flexible lithium ion batteries. *Electrochim. Acta* **2022**, *423*, 140595. [[CrossRef](#)]
56. Joshi, B.; Samuel, E.; Kim, Y.-i.; Yarin, A.L.; Swihart, M.T.; Yoon, S.S. Progress and potential of electrospinning-derived substrate-free and binder-free lithium-ion battery electrodes. *Chem. Eng. J.* **2022**, *430*, 132876. [[CrossRef](#)]
57. Zhang, L.; Qin, X.; Zhao, S.; Wang, A.; Luo, J.; Wang, Z.L.; Kang, F.; Lin, Z.; Li, B. Advanced Matrixes for Binder-Free Nanostructured Electrodes in Lithium-Ion Batteries. *Adv. Mater.* **2020**, *32*, 1908445. [[CrossRef](#)]
58. Jain, R.; Lakshnot, A.S.; Bhimani, K.; Sharma, S.; Mahajani, V.; Panchal, R.A.; Kamble, M.; Han, F.; Wang, C.; Koratkar, N. Nanostructuring versus microstructuring in battery electrodes. *Nat. Rev. Mater.* **2022**, *7*, 736–746. [[CrossRef](#)]
59. Zhen, E.; Jiang, J.; Lv, C.; Huang, X.; Xu, H.; Dou, H.; Zhang, X. Effects of binder content on low-cost solvent-free electrodes made by dry-spraying manufacturing for lithium-ion batteries. *J. Power Source* **2021**, *515*, 230644. [[CrossRef](#)]
60. Wood, D.L.; Li, J.; Daniel, C. Prospects for reducing the processing cost of lithium ion batteries. *J. Power Source* **2015**, *275*, 234–242. [[CrossRef](#)]
61. He, X.; Hu, Y.; Shen, Z.; Chen, R.; Wu, K.; Cheng, Z.; Zhang, X.; Pan, P. GeOx ultra-dispersed in microporous carbon nanofibers: A binder-free anode for high performance lithium-ion battery. *Electrochim. Acta* **2017**, *246*, 981–989. [[CrossRef](#)]
62. Chen, K.-T.; Chang, W.-C.; Yang, H.-J.; Tsai, C.-Y.; Huang, S.-B.; Tuan, H.-Y. Free standing Si (Ge) nanowire/Cu nanowire composites as lithium ion battery anodes. *J. Taiwan Inst. Chem. Eng.* **2019**, *104*, 54–64. [[CrossRef](#)]
63. Wang, S.; Liu, D.; Cai, X.; Zhang, L.; Liu, Y.; Qin, X.; Zhao, R.; Zeng, X.; Han, C.; Zhan, C.; et al. Promoting the reversibility of lithium ion/lithium metal hybrid graphite anode by regulating solid electrolyte interface. *Nano Energy* **2021**, *90*, 106510. [[CrossRef](#)]
64. Wu, Q.; Yang, J.; Zhao, Y.; Song, R.; Wang, Z.; Huang, Z.; Shi, M.; Ye, Y.; He, D.; Mu, S. Lifting the energy density of lithium ion batteries using graphite film current collectors. *J. Power Source* **2020**, *455*, 227991. [[CrossRef](#)]
65. Yang, Y.; Yuan, W.; Zhang, X.; Ke, Y.; Qiu, Z.; Luo, J.; Tang, Y.; Wang, C.; Yuan, Y.; Huang, Y. A review on structuralized current collectors for high-performance lithium-ion battery anodes. *Appl. Energy* **2020**, *276*, 115464. [[CrossRef](#)]
66. Dayer, A.; Feschotte, P. Les systèmes binaires cobalt-germanium et nickel-germanium: Étude comparée. *J. Less Common Met.* **1980**, *72*, 51–70. [[CrossRef](#)]
67. Liu, X.; Liu, Y.-S.; Harris, M.M.; Li, J.; Wang, K.-X.; Chen, J.-S. Germanium nanoparticles supported by 3D ordered macroporous nickel frameworks as high-performance free-standing anodes for Li-ion batteries. *Chem. Eng. J.* **2018**, *354*, 616–622. [[CrossRef](#)]
68. Erdemir, F.; Güler, O.; Çanakçı, A. Electroless nickel-phosphorus coated expanded graphite paper: Binder-free, ultra-thin, and low-cost electrodes for high-performance supercapacitors. *J. Energy Storage* **2021**, *44*, 103364. [[CrossRef](#)]
69. Liu, B.-L.; Ma, Y.-X.; Wang, J.-W.; Kang, X.-Y.; He, L.-J.; Lei, L.; Ran, F. Fabrication of nickel cobalt bimetallic sulfide doped graphite carbon nanohybrids as electrode materials for supercapacitors. *Diam. Relat. Mater.* **2022**, *124*, 108955. [[CrossRef](#)]
70. Uddien Shaik, R.; Karanjai, M.; Joardar, J.; Hebalkar, N.Y.; Borse, P.H. Thermally stable electro catalytic nickel-phosphide film deposition on graphite for HER electrode application. *Mater. Sci. Eng. B* **2022**, *285*, 115927. [[CrossRef](#)]
71. Su, Z.; Zhang, S.-h.; Wu, J.-j. Effect of nickel-plated graphite on microstructure and properties of matrix for Fe-based diamond tools. *Trans. Nonferrous Met. Soc. China* **2022**, *32*, 1575–1588. [[CrossRef](#)]
72. Hao, Z.; Kochubei, S.A.; Popov, A.A.; Volodin, V.A. On Raman scattering cross section ratio of amorphous to nanocrystalline germanium. *Solid State Commun.* **2020**, *313*, 113897. [[CrossRef](#)]
73. Wang, L.; Liu, Z.; Guo, Q.; Yang, J.; Dong, X.; Li, D.; Liu, J.; Shi, J.; Lu, C.; Liu, L. Structure of silicon-modified mesophase pitch-based graphite fibers. *Carbon* **2015**, *94*, 335–341. [[CrossRef](#)]

74. Wang, H.; Guo, Q.; Yang, J.; Zhao, Y.; Wang, X.; Tao, Z.; Liu, Z.; Feng, Z.; Liu, L. Microstructure and thermophysical properties of B₄C/graphite composites containing substitutional boron. *Carbon* **2013**, *52*, 10–16. [[CrossRef](#)]
75. Wang, H.; Guo, Q.; Yang, J.; Liu, Z.; Zhao, Y.; Li, J.; Feng, Z.; Liu, L. Microstructural evolution and oxidation resistance of polyacrylonitrile-based carbon fibers doped with boron by the decomposition of B₄C. *Carbon* **2013**, *56*, 296–308. [[CrossRef](#)]
76. Yuan, Y.; Pan, Y.-T.; Zhang, Z.; Zhang, W.; Li, X.; Yang, R. Nickle nanocrystals decorated on graphitic nanotubes with broad channels for fire hazard reduction of epoxy resin. *J. Hazard. Mater.* **2021**, *402*, 123880. [[CrossRef](#)] [[PubMed](#)]
77. Su, X.; Sun, B.; Wang, J.; Zhang, W.; Ma, S.; He, X.; Ruan, H. Fast capacity estimation for lithium-ion battery based on online identification of low-frequency electrochemical impedance spectroscopy and Gaussian process regression. *Appl. Energy* **2022**, *322*, 119516. [[CrossRef](#)]

Disclaimer/Publisher's Note: The statements, opinions and data contained in all publications are solely those of the individual author(s) and contributor(s) and not of MDPI and/or the editor(s). MDPI and/or the editor(s) disclaim responsibility for any injury to people or property resulting from any ideas, methods, instructions or products referred to in the content.